An edge-based strain smoothing particle finite element method for large deformation problems in geotechnical engineering

Yin-Fu JIN[1], Wei-Hai YUAN[2], Zhen-Yu YIN[1*] and Yung-Ming CHENG[1]

Affiliation:

1 Department of Civil and Environmental Engineering, The Hong Kong Polytechnic University, Hung Hom, Kowloon, Hong Kong

2 College of Mechanics and Materials, Hohai University, Nanjing, China (yuanwh@hhu.edu.cn)

* Corresponding author: Dr Zhen-Yu Yin, Tel. +852 34008470, Fax +852 23346389, E-mail: zhenyu.yin@polyu.edu.hk; zhenyu.yin@gmail.com

Abstract: To solve large deformation geotechnical problems, a novel strain-smoothed particle finite element method (SPFEM) is proposed that incorporates a simple and effective edge-based strain smoothing method within the framework of original PFEM. Compared to the original PFEM, the proposed novel SPFEM can solve the volumetric locking problem like previously developed node-based smoothed PFEM when lower-order triangular element is used. Compared to the node-based smoothed PFEM known as ''overly soft'' or underestimation property, the proposed SPFEM offers super-convergent and very accurate solutions due to the implementation of edge-based strain smoothing method. ~~The advantage of the novel method is to use very simple lower-order triangular element without suffering from volumetric locking via the strain smoothing method, instead of the higher-order triangular element/mixed stabilised formulation in the original PFEM, while preserving the same calculation accuracy.~~ To guarantee the computational stability, the proposed SPFEM uses an explicit time integration scheme, and adopts an adaptive updating time step. Performance of the proposed SPFEM for geotechnical problems is first examined by four benchmark numerical examples: (1) bar vibrations, (2) large settlement of strip footing, (3) collapse of aluminium bars column and (4) failure of a homogeneous soil slope. Finally, the progressive failure of slope of sensitive clay is simulated using the proposed SPFEM to show its outstanding performance in solving large deformation geotechnical problems. All results demonstrate that the novel SPFEM is a powerful and easily extensible numerical method for analysing large deformation problems in geotechnical engineering.

Key words: strain smoothing; finite element method; large deformation; slope failure; footing; soil collapse

1 Introduction

In geotechnical engineering, numerous problems involve large deformation, such as installation of foundations [1-4], landslides [5] and debris flow [6]. Benefitted from the sustained development of computing power, numerical simulations have become standard methods in geomechanics and its related fields. Among those numerical methods, the finite element method (FEM) features prominently in engineering practices [1, 3, 7-12]. For FEM, however, excessive deformation of a mesh can result in numerical inaccuracies, even to the point of making calculation impossible for large deformation problems. Many researchers adopt continuous remeshing and mapping of stresses from the old elements to the new elements method to solve very large deformation (using commercial finite element programs with purpose developed submodules), but such methods are quite tedious and time-consuming to be performed.

A number of numerical methods have been developed to help tackling the large deformation problems, which can be generally divided into three categories: discontinuous, continuous and coupled continuous–discontinuous approaches. In contrast to the continuous approaches, practical applications of discontinuous approaches are limited by their burdensome computational cost, although the robustness and potential of such methods have been demonstrated in academic exercises. Continuous approaches can be roughly divided into three groups: (1) mesh-based methods, such as ~~arbitrary Lagrangian–Eulerian (ALE) [13] and~~ the remeshing and interpolation technique with small strain (RITSS) [13]; (2) mesh-free particle methods, such as smoothed particle hydrodynamics (SPH) [14] and element-free Galerkin (EFG) [15]; and (3) mesh-based particle methods, such the material point method (MPM) [16] and particle finite element method (PFEM)[17]. Beyond the foregoing approaches, the coupled Eulerian–Lagrangian (CEL) is another mesh-based method [18, 19], similar to MPM and requires a background mesh. Although both ALE and RITSS have been used to solve problems involving relatively large deformations, both methods fail when the original boundaries change during the deformation process [20]. For SPH, EFG, MPM and CEL, applying boundary conditions is difficult – and, moreover, is always inaccurate when solving small-deformation problems or during the early stages of large-deformation problems. By contrast, PFEM which is developed to solve fluid–structure interaction problems (Oñate et al. [17,

21, 22]) and fluid only problems [23, 24] can be employed as an ideal method for avoiding the aforementioned problems, and has recently been used to solve problems in geomechanics [25-33]. The key feature of PFEM is that nodes are regarded as "particles" and the continuum medium as a cloud of these particles, which transport all the information of the continuum medium (e.g., displacements, strains, stresses, material properties, state variables), allow free movement and even separation from the continuum to which they originally belong. Indeed, the PFEM is actually an updated Lagrangian approach with frequent remeshing, based on the Delaunay triangulation technique, to overcome mesh distortion problems. As such, it inherits both the flexibility of mesh-free particle methods for arbitrary changes in geometry and the solid mathematical foundation of the traditional FEM.

For various applications of PFEM, 6-node (~~quadrilateral~~ quadratic) triangle elements are always used in geotechnical applications (Zhang et al. [20, 27, 29, 34]). When seeking to reduce the computational cost, low-order finite elements such as 3-node triangular elements are very attractive for their simplicity and efficiency. However, in general, the accuracy of low-order elements is not sufficient for use in engineering practice because of the problem of volumetric locking (also called the zero-energy or hourglass effect). With a view to improve the accuracy of low-order elements while preserving their advantages, the strain smoothing technique has been developed to smooth the strain field [35] and has been successfully applied to various mechanics problems [35]. Although mixed stabilised formulations [36, 37] can also overcome the volumetric locking effect of the 3-node triangle element, implementation is difficult because of the more complex equations required than for strain smoothing methods. The smoothing domains can be constructed on the basis of a cell, node, edge or face; thus cell-based, node-based, edge-based and face-based smoothed-FEM (S-FEM) methods were devised [35]. Compared to the standard FEM, S-FEM achieves significantly improved accuracy, especially for 3-node triangular elements. The important advantage of S-FEM is that no additional degrees of freedom (DOFs) are required. As a result, the strain smoothing method can also be used in the original PFEM to reduce the computational cost. In fact, the implementation of strain smoothing in the original PFEM has already been conducted by Zhang et al. [26] implicitly and Yuan et al. [25] explicitly, adopting a node-based strain smoothing technique for nodal integration

proposed by Liu et al. [38]. However, among various smoothing methods, the edge-based S-FEM is generally known to be the most effective [39, 40]. Thus the edge-based strain smoothing technique is worth incorporating into original PFEM to improve accuracy while simultaneously reducing the computational cost. If so, only very simple lower-order triangular element can be directly adopted without suffering volumetric locking via the strain smoothing method, instead of using the higher-order triangular element/mixed stabilised formulation in original PFEM.

In this study, within the PFEM framework, a newly developed edge-based strain smoothing technique (the strain-smoothed element method) for 3-node triangle elements is incorporated and an SPFEM with explicit time integration scheme is then developed. Next, four benchmark tests are conducted to verify the correctness of the program's implementation, the effectiveness of the adopted edge-based strain smoothing technique and the feasibility of the proposed SPFEM for large-deformation problems: (1) bar vibrations, (2) settlement of strip footing, (3) collapse of aluminium bars column and (4) failure of a homogeneous soil slope. Finally, the proposed SFPEM is applied to simulate the progressive failure of slope of sensitive clay.

2 Explicit edge-based smoothed particle finite element method

2.1 Particle Finite Element Method (PFEM)

In PFEM, the domain of the problem is first discretised into a cloud of particles. Then, on the basis of particles, the triangle elements are generated through Delaunay triangulation and the alpha-shape technique is used to remove elements that do not meet the requirements. Next, the governing equations are solved using a standard finite element method, such as the Newton–Raphson procedure [30]. Apart from the standard PFEM method, the explicit time integration procedure [25] and mathematical programming [20, 29, 34] can also be adopted to solve the governing equations. Finally, information related to particles is updated and the convergence criterion is checked. Fig. 1 depicts the main procedures of PFEM. The details of original PFEM can be found in [27, 28, 30].

2.2 Momentum balance equation

The divergence theorem can be employed to give:

$$\int_V \left(\nabla \cdot \boldsymbol{\sigma} + \rho \mathbf{g} - \rho \mathbf{a}\right) dV = \mathbf{0} \tag{1}$$

With stress vector $\boldsymbol{\sigma}$ and gravity acceleration assembled in the vector $\mathbf{g}$ the linear momentum balance of a body V with boundary S reads:

$$\int_S \mathbf{n}\cdot\boldsymbol{\sigma}dS + \int_V \rho\mathbf{g}dV = \int_V \rho\mathbf{a}dV \tag{2}$$

where ρ is the material density, $\mathbf{n}$ is the outward unit vector at the boundary of the body, and $\mathbf{a}$ is the acceleration.

By taking the principle of virtual displacement, the equilibrium equation expressed in the weak form is given:

$$\int_V \left(\rho\delta\mathbf{u}^T\mathbf{a} + \left(\mathbf{L}\delta\mathbf{u}\right)^T\boldsymbol{\sigma}\right)dV = \int_S \delta\mathbf{u}^T\mathbf{t}_s dS + \int_V \rho\delta\mathbf{u}^T\mathbf{g}dV \tag{3}$$

in which $\mathbf{u}$ is the test function, which is assumed to satisfy $\delta\mathbf{u}=0$ where the displacement boundary conditions are prescribed, and $\mathbf{t}_s$ is the prescribed traction. $\mathbf{L}$ is operator matrix expressed as

$$\mathbf{L}^T = \begin{bmatrix} \frac{\partial}{\partial x} & 0 & 0 & \frac{\partial}{\partial y} & 0 & \frac{\partial}{\partial z} \\ 0 & \frac{\partial}{\partial y} & 0 & \frac{\partial}{\partial x} & \frac{\partial}{\partial z} & 0 \\ 0 & 0 & \frac{\partial}{\partial z} & 0 & \frac{\partial}{\partial y} & \frac{\partial}{\partial x} \end{bmatrix} \tag{4}$$

To solve Eq.(3), it must be spatially discretised by finite elements. Similar to solve the standard FEM problem, an ~~the~~ explicit time integration scheme ~~will~~ can be adopted ~~for such purpose~~.

2.3 Adopted edge-based strain smoothing method

To overcome the volumetric locking problem caused by the strain constant in 3-node triangular elements, a simple and effective strain smoothing method (the strain-smoothed element method) for 3-node triangular elements, developed by Lee and Lee [39] was employed in the original PFEM. Using the adopted strain smoothing method, the strains of all neighbouring elements are fully used in the strain smoothing process. For 3-node triangular elements, the strains of up to three surrounding elements can be used through element edges (see Fig. 2a), where $\boldsymbol{\varepsilon}^{(e)}$ is the strain of a target element and $\boldsymbol{\varepsilon}^{(k)}$ is the strain of the kth neighbouring element. Thus, the smoothed strains between the target element and neighbouring elements are defined as

$$\hat{\boldsymbol{\varepsilon}}^{(k)} = \frac{1}{A^{(e)} + A^{(k)}} \left(A^{(e)} \boldsymbol{\varepsilon}^{(e)} + A^{(k)} \boldsymbol{\varepsilon}^{(k)} \right), \text{ with } k = 1, 2, 3 \tag{5}$$

where $A^{(e)}$ and $A^{(k)}$ are the areas of the target element and the kth neighbouring element, respectively, as can be seen in Fig. 2(b). Note that if the kth edge of the target element corresponds to a boundary, there is no neighbouring element for the edge and $\hat{\boldsymbol{\varepsilon}}^{(k)} = \boldsymbol{\varepsilon}^{(e)}$ is thus adopted.

In the 3-node triangular element, three point Gauss integration is used to calculate the stiffness matrix and the external force. As shown in Fig. 2(d), the smoothed strain values in Eq.(5) are directly assigned to the Gauss points (a, b, and c in Fig. 2c) of the target element using the following equations,

$$\begin{aligned} \boldsymbol{\varepsilon}^{a} &= \frac{1}{2}\left(\hat{\boldsymbol{\varepsilon}}^{(1)} + \hat{\boldsymbol{\varepsilon}}^{(3)} \right) \\ \boldsymbol{\varepsilon}^{b} &= \frac{1}{2}\left(\hat{\boldsymbol{\varepsilon}}^{(1)} + \hat{\boldsymbol{\varepsilon}}^{(2)} \right) \\ \boldsymbol{\varepsilon}^{c} &= \frac{1}{2}\left(\hat{\boldsymbol{\varepsilon}}^{(2)} + \hat{\boldsymbol{\varepsilon}}^{(3)} \right) \end{aligned} \tag{6}$$

Note that in the adopted edge-based strain smoothing method, exterior (boundary) elements have fewer neighbouring elements than interior elements; thus the strain smoothing effect in the exterior region could be less than that in the interior region.

According to Lee and Lee [39], the 3-node triangular elements subject to the edge-based strain smoothing method pass all the basic tests (patch, isotropy and zero-energy mode tests). Thus the edge-based strain smoothing method shows ~~satisfactory~~ best performance among the various S-FEM methods [39]. We thus selected this method to improve the accuracy of the PFEM calculation.

2.4 Explicit time integration and adaptive time step

For the implicit PFEM [27]/SPFEM [26] schemes, a large part of the computing time is spent in the solution of the linear systems. On the contrary, no linear systems have to be solved when adopting the explicit approach, but obviously a smaller time step is necessary. According to [41, 42], the explicit scheme is more efficient than implicit scheme for large scale problems, where the computational cost increases approximately linearly with the number of freedoms.

Therefore, the explicit time integration scheme is used for two primary reasons: (1) ease of implementation and (2) ability to avoid massive computation loads when dealing with large-scale

problems. One of the most popular explicit time integration schemes approximating velocity at mid-interval (Belytschko et al. [43]) is employed. The algorithm is summarised in the following box.

Initialise velocities $\dot{\mathbf{a}}^0$ and accelerations $\ddot{\mathbf{a}}^0$

Compute the lumped mass matrix: $\mathbf{M}$

Compute: $\dot{\mathbf{a}}^{\frac{1}{2}t} = \dot{\mathbf{a}}^0 + \frac{1}{2}\Delta t \ddot{\mathbf{a}}^0$

For each time step:

1. Solve for total displacements: $\mathbf{a}^{t+\Delta t} = \mathbf{a}^t + \Delta t \dot{\mathbf{a}}^{t+\frac{1}{2}\Delta t}$
2. Compute the displacement increment: $\Delta \mathbf{a} = \mathbf{a}^{t+\Delta t} - \mathbf{a}^t$
3. For each integration point i:
   - Compute the strain increment: $\Delta \mathbf{a} \rightarrow \Delta \boldsymbol{\varepsilon}_i$
   - Compute the stress increment: $\Delta \boldsymbol{\varepsilon}_i \rightarrow \Delta \boldsymbol{\sigma}_i$
   - Compute the total stress: $\boldsymbol{\sigma}_i^{t+\Delta t} = \boldsymbol{\sigma}_i^t + \Delta \boldsymbol{\sigma}_i$
4. Compute the internal force vector: $\mathbf{f}_{\text{int}}^{t+\Delta t} = \sum_{e=1}^{n_e} \sum_{i=1}^{n_i} \omega_i \det(\mathbf{J}_i) \mathbf{B}_i^{\mathrm{T}} \boldsymbol{\sigma}_i$
5. Solve for the new accelerations: $\ddot{\mathbf{a}}^{t+\Delta t} = \mathbf{M}^{-1}\left(\mathbf{f}_{\text{ext}}^{t+\Delta t} - \mathbf{f}_{\text{int}}^{t+\Delta t}\right)$
6. Compute the velocities at new mid-time: $\dot{\mathbf{a}}^{t+\frac{3}{2}\Delta t} = \dot{\mathbf{a}}^{t+\frac{1}{2}\Delta t} + \Delta t \ddot{\mathbf{a}}^{t+\Delta t}$

Explicit time integration schemes have the advantage of reducing computational effort especially if a lumped mass matrix is used, as factorisation and storage of a system matrix are then not required. Two possible disadvantages of explicit time integration schemes are the stability of the solution and the impossibility of ascertaining whether the solution computes the 'dynamic equilibrium path' with sufficient accuracy. That explicit time stepping schemes are only conditionally stable which implies that the time step size must be smaller than a critical value to ensure the computation stability, with that value is given by

$$\Delta t_{\text{stable}} = \alpha \frac{l_{\min}}{c} \tag{7}$$

where Δt_{stable} is the critical time step size, l_{min} is the characteristic length of the element. For a triangular element, l_{min} is the minimum height for all triangle elements; c is the speed of the wave propagation which can be approximately estimated by $c = \sqrt{(\lambda + 2\mu)/\rho}$ (where ρ is material density, and λ and μ are two Lamé's constants); and α is the reduction factor, which usually

equals $1/\sqrt{2}\sim1.0$ according to ABAQUS [44]. Typically $\alpha=0.9$ can be adopted. In this study, a smaller reduction factor α=0.7 is adopted for a stable calculation. Because the characteristic length of the element is changing during the simulation, the adaptive time step scheme is used. Note that the time step size depending on the mesh size is changing due to the rebuild of mesh in SPFEM.

2.5 Computational cycle of proposed SPFEM

A typical computational cycle for the proposed SPFEM is similar to that for the classical PFEM, as shown in Fig. 1. Incorporating the edge-based strain smoothing method ~~and bulk viscosity~~, the main procedure of the proposed SPFEM can be simply written as follows:

(1) Discretise the domain into a set of nodes/particles.

(2) Build the computational mesh using the Delaunay triangulation technique.

(3) Define the domain boundary using an alpha-shape method.

(4) Transfer the information of variables (stresses and state variables of constitutive model) from Gauss points to nodes by the superconvergent patch recovery scheme [45].

(5) Solve the governing equations using explicit time integration scheme, get the incremental strains of each element ($\Delta\varepsilon=B\Delta u$) and then smooth the strains for each element using the edge-based strain smoothing technique, update the stresses via a constitutive model ($\sigma\_new=\sigma\_old+\Delta\varepsilon D$) ~~and apply the bulk viscosity for calculating internal force~~.

(6) Transfer the updated stresses and state variables of constitutive model at Gauss integration points to nodes, and then update the information of nodes (the position and the transferred stresses and state variables) preparing for the new mesh of next time step.

(7) Check the convergence criterion: if met, stop; otherwise, return to step (2).

Note that another available remapping approach is the Unique Element Method (UEM). This method maps the variables from the Gauss integration points belonging to old mesh to the Gauss integration points belonging to new mesh directly. More details about UEM can be found in [13] for readers with interesting.

Following the proposed procedure, existing FEM codes can be easily changed to SPFEM.

3 Numerical examples

To examine the proposed SPFEM, the linear elastic model and perfect elasto–plastic Mohr–Coulomb (MC) model were implemented. Four benchmark examples were tested in this study: (1) axial vibration of a continuum bar using the elastic model, (2) penetration of rigid footing in soft soil using the Tresca model reduced from the MC model (c'=1 kPa, ϕ=0°, E=100 kPa, υ=0.495 and ψ=0°), (3) collapse of an aluminium bar column using the MC model and (4) failure of a homogeneous soil slope using the MC model.

3.1 Constitutive model

The classic Mohr–Coulomb (MC) model under the framework of elastoplasticity was adopted. The elastic part is general Hook's law requiring two input parameters (Young's modulus E and Poisson's ratio ν), and plastic part follows the non-associated flow rule with three parameters (friction angle ϕ, cohesion c and dilation angle ψ). The Mohr–Coulomb yield criterion f and plastic potential g are written in principal stresses as follow

$$f = (\sigma_1 - \sigma_3) + (\sigma_1 + \sigma_3)\sin\phi - 2c\cos\psi \tag{8}$$

$$g = (\sigma_1 - \sigma_3) + (\sigma_1 + \sigma_3)\sin\psi \tag{9}$$

Due to the existence of apex point at the yield surface, the integration solution of MC model is always a problem. According to Clausen et al.[46], an efficient return algorithm for stress update in numerical plasticity computations was adopted for numerically integrating the non-associated Mohr–Coulomb model. The source code for MC model used in following cases is available at http://alum.sharif.ir/~koohsari/doc/M-C_by_Johan_Clausen.for. All readers who are interesting on large deformation simulation can reproduce the presented cases by the proposed SPFEM with this MC model.

3.2 Validation examples

3.2.1 *Axial vibration of a continuum bar*

In this case, the dynamic vibration of a continuum bar is simulated as a benchmark test to examine the correctness of a proposed SPFEM. Fig. 3 shows the geometry and mesh of the bar. In the first stage, at the right side of bar only a vertical velocity 0.1 m/s is applied, and then let the bar

vibrate freely for 10 seconds. Note that no external force is applied during this vibration. In the simulation, the plane strain condition is assumed and the bar is considered to be elastic material with the following parameters: Young's modulus E=100 kPa, density ρ=1000 kg/m^3. The gravitational acceleration is set to be zero, which means the weight of the beam is neglected. The left side of bar is fixed and the right side free. The top and bottom sides are free only in the horizontal directions. The analytical solution for the velocities and displacements are given as

$$\begin{aligned} v(x,t) &= v_0 \cos(\omega_1 t)\sin(\beta_1 x) \\ u(x,t) &= \frac{v_0}{\omega_1}\sin(\omega_1 t)\sin(\beta_1 x) \end{aligned} \tag{10}$$

where v_0 is the size of initial velocity. $\beta_1 = \pi/2L$ and $\omega_1 = \beta_1 c$, where $c = \sqrt{E/\rho}$ is the elastic wave speed. Initial velocity and displacements are given by

$$\begin{aligned} v(x,0) &= v_0 \sin(\beta_1 x) \\ u(x,0) &= 0 \end{aligned} \tag{11}$$

Fig. 4 compares the velocity and displacement between the analytical solution and simulation. Good agreement between the analytical solution and simulation are obviously found, demonstrating the correctness of SPFEM and its capability to simulate dynamic solid structure behaviours.

3.2.2 *Penetration of rigid footing in soft soil*

This numerical example considers a rough rigid strip footing penetrating an elastic–perfectly plastic soil which is assumed to be weightless. Because this case has been simulated using various numerical methods with the availability of analytical solutions, a comparison between the proposed SPFEM and other solutions can validate the correctness of the SPFEM.

Fig. 5 shows the geometry and mesh of the footing problem. The width of strip foundation B is assumed to be 2.0 m, while the rest of the dimension is 5B wide and deep, to reduce the boundary effect. A plane stain condition for the simulation is assumed. Because of the symmetry, only half the geometry of the problem is considered, with the boundary conditions properly applied along the symmetry plane. The bottom side is fixed in the horizontal and vertical directions, whereas the right hand side is fixed only in the horizontal direction. To guarantee both numerical accuracy and computational efficiency, a non-uniform initial particle distribution is assumed. The domain is

discretized into 6629 particles, and the initial number of elements is 12209, dense enough to obtain accurate and stable results.

Due to the non-uniform mesh size, it is difficult to apply alpha shape technique to the whole model. Therefore, the alpha shape technique is only applied to the region where the large deformation occurs. In this case, the region applied alpha shape is shown in Fig. 5. In this region, the mesh size is almost uniform and is easy to use the alpha shape technique.

In the simulation, the penetration speed is set to 0.01 m/s. Thus a total of 200 s would be required for a final depth of 2.0 m, which is consistent with other simulations using different techniques [47-49]. The soil underneath the rigid footing is modelled by the elastic–perfectly plastic Tresca model with the following parameters: unit weight γ=16 kN/m^3, Young's modulus E=100 kPa, Poisson's ratio υ=0.495 and undrained shear strength c_u=1 kPa.

The results, in terms of a normalized vertical reaction force versus penetration depth, are shown in Fig. 6. Note that the unsmooth curve (blue line) of the resistance force is related to errors introduced during the remeshing process, which changes element topology relations and thus the elements connected to the particles, as well as the area of the strain smoothing cells. Since the SPFEM adopts the explicit integration scheme rather than the standard PFEM using the implicit integration scheme, it is reasonable that oscillations of the blue curve by SPFEM seem larger with respect to the oscillations of the curve of the standard PFEM. This can also be found in various calculations and comparisons [4, 19, 25]. For a large deformation calculation in geotechnical engineering, especially using an explicit time integration method, this numerical error is acceptable. The obtained result is also compared to various reference solutions (da Silva et al. [50], Prandtl [51] and Meyerhof [52]) and other numerical solutions (PFEM [47], MPM [53], ALE [54], iSPFEM [26] and eSPFEM [25] using a node integration scheme). All results are located between the analytical solution obtained by Prandtl [51] ($(\pi+2)c_u = 5.14c_u$) and the limit load obtained by Meyerhof [52] ($(2\pi+2)c_u = 8.28c_u$). It is apparent that the obtained curve is closer to the solutions obtained by PFEM [47], MPM [53] and ALE [54]. Note that the proposed SPFEM solution is obtained using 3-node triangular elements, without the use of mixed stabilized formulations or high-order elements to overcome volumetric locking. The results demonstrate that the SPFEM with 3-node triangular

elements has the same simulation accuracy with the original PFEM with 6-node triangular elements. Thus the proposed SPFEM is superior to the original PFEM when directly adopting low-order triangular elements without suffering from volumetric locking.

Furthermore, the obtained curve is higher than the eSPFEM [25] and iSPFEM [26] solutions, which is attributed to the difference of adopted strain smoothing techniques. In eSPFEM [25] and iSPFEM [26], the node-based strain smoothing method is adopted, which is known as ‘‘overly soft’’ or underestimation property and thus offers a upper bound solution [25, 26, 40]. In the proposed SPFEM, the edge-based strain smoothing method is used, which has a close-to-exact stiffness and often offers super-convergent and very accurate solutions [40]. Note that the Prandtl plasticity solution is obtained under small deformation condition so that and the computed result by SPFEM is higher than that because of large deformation.

Fig. 7 shows the contours of vertical displacement, horizontal displacement, the equivalent plastic strain $\varepsilon_q^p = \sqrt{2\left(\boldsymbol{\varepsilon}^p : \boldsymbol{\varepsilon}^p\right)/3}$ as well as the shear stress τ_{xy}, where $\boldsymbol{\varepsilon}^p$ is the plastic strain tensor. Fig. 7c shows a wedge-shaped zone developed below the footing: inside the wedge, elastic behaviour is dominant, but there is a transition zone below and on the side of the footing, where significant plastic strain develops. Fig. 7d shows below the footing corner a region of shear stress concentration with a maximum value exactly equal to the cohesion of the soil, assuming a weightless and frictionless soil. A wing-shaped shear stress bulb develops next to the corner of the footing and spreads out upwards into the soil, and the shear stress region shows a minimum value of –1.0 kPa.

For further showing robustness of the proposed SPFEM to capture the footing failure problem, the same problem was simulated using the Von-Mises model with the following parameters: Shear modulus G=1000 kPa, Poisson’s ratio υ=0.49 and undrained shear strength c_u=10 kPa in order to be comparable to the analytical solution (Prandtl [51]) and the simulated results by Qiu et al.[55]. Fig. 8 shows the comparison that all simulated results are located between the analytical solution obtained by Prandtl [51] and the limit load obtained by Meyerhof [52]. Moreover, the obtained curve is closer to the solutions obtained by Qiu et al.[55] using different modules of ABAQUS. Therefore, the proposed SPFEM is robust to capture the failure problems.

3.2.3 *Collapse of aluminium bar column*

To further demonstrate the proposed method's ability to solve large deformation geotechnical problems, the rectangular channel soil collapse tests conducted by Bui et al. [56] are analysed and the results compared with the experimental data and other numerical solutions (i.e., MPM [57] and SPH [58]). In the experiments, small aluminium bars of various diameters (0.1 and 0.15 cm) are used to model the soil. The bars are initially arranged into an area 20 cm long × 10 cm high × 2 cm wide, delimited by two flat solid walls. The experiment begun by quickly moving the right wall horizontally to the right, causing the aluminium bars to flow to the side due to gravity loading. The details of the experimental setup are given in [59] and shown in Fig. 9.

In the simulation, a two-dimensional plain strain condition is assumed. The material behaviour of the aluminium bars is simulated using the Mohr–Coulomb (MC) model. According to Bui et al. [56], the following material parameters corresponding to MC are used: shear modulus, G=0.7 MPa; Poisson's ratio, υ=0.3; density, ρ=2.650×10^3 kg/m^3; cohesion, c=0 kPa; friction angle, ϕ=19.8°; dilatancy angle, ψ=0°. The simple rigid plastic Coulomb interface model by controlling interface frictional coefficient $\mu = \tan(\phi_{int})$ between the aluminium bars and the rigid bottom surface is implemented into the code. The value of μ = 0.36 corresponding to the same friction angle of aluminium bars is used in the simulation. The analysis is conducted in two stages: first, roller support is assumed on both sides of the column, and the bottom boundary is fully fixed, rendering the specimen initial stresses generated by gravity loading; second, the right-side wall is assumed to be removed instantaneously when the experiment starts, allowing the column to collapse from that side. The domain is discretized into 6327 particles, and the initial number of elements is 12268.

Fig. 10 shows the final configuration of soil collapse simulated by proposed SPFEM. The final surface configurations and failure lines are compared with the experimental results and two numerical simulations (MPM [57] and SPH [58]), as shown in Fig. 11. All numerical results show a very similar response, and good agreement can be found between numerical and experimental results.

3.2.4 *Failure of a homogeneous soil slope*

In this case, the failure of a homogeneous soil slope is analysed and the feasibility of the proposed SPFEM is also verified. The geometric description and initial mesh of this problem is given in Fig. 12.

The soil behaviour is modelled by an elastic–perfectly plastic Mohr–Coulomb material, and the following material properties are used: Young's modulus of E=100 MPa and Poisson's ratio of υ=0.3, with shear strength parameters a cohesion of c_0=10 kPa and a friction angle of ϕ_0=20°. The dilation angle is taken to be ψ=0°, and the unit weight is γ=20 kN/m^3. The same problem has been analysed by Griffiths and Lane [60] using a small-deformation FEM and by Zhang et al. [26] using an implicit SPFEM.

To analyse slope stability with the shear strength reduction technique, a series of shear strength parameters are estimated, defined by

$$c=\frac{c_0}{\mathrm{SRF}} \qquad \phi=\arctan\left(\frac{\tan\phi_0}{\mathrm{SRF}}\right) \tag{12}$$

where SRF=shear strength reduction factor. For each simulation, 3513 particles are used to discretize the problem domain with 6191 elements initially – enough to obtain results that qualify as accurate when compared to the same case using iSPFEM [26]. The loading time for all cases is 5 s.

The critical value of SRF that causes the failure of slope is considered to be the factor of safety (FOS) of this slope. According to Griffiths and Lane [60], a critical value of the SRF between 1.30 and 1.40 was found for the small-deformation stage. Thus, to investigate the simulated performance of proposed SPFEM, a series of simulations with SRF=1.2, 1.3, 1.4, 1.5 and 1.6 was conducted and different variables (such as equivalent plastic strain and vertical stress) compared for different simulations at final loading time. Fig. 13 shows the evolution of the horizontal displacement at top of slope with different SRF values. The critical value of the SRF obtained by SPFEM agrees well with that found by Griffiths and Lane [60], demonstrating the effectiveness of the proposed method. Fig. 14 shows the final configurations and the equivalent plastic strain invariants for different values of SRF. When SRF=1.3, the band of plastic strain localization occurs but does not connect through the whole slope from toe to top – meaning that the slope is safe. When SRF$\geqslant$1.40, a continuous band of

plastic strain localization is detected. Moreover, the localized failure is accompanied by a large increment of displacement. Occurrence of slope failure is thus proved. Comparing Fig. 14(a) with Fig. 14(b) shows that the failure occurs first at the slope toe and subsequently extends to the slope top, itis clear that when using the proposed SPFEM, highly distorted configurations induced by large deformation can be easily taken into consideration and the geometry of the final deposit predicted rationally.

The preliminary results demonstrate that an accurate FOS can be obtained by the proposed SPFEM. To demonstrate the ability to model slope failure involving large deformation, simulation was performed with SRF=2.0 (corresponding to ϕ=10° and c=5 kPa). Fig. 15 compares initial and final configurations of slope as well as equivalent plastic strain distribution. It is apparent that slope failure involving large deformation can also be well solved by the proposed SPFEM.

3.3 Illustrative example

To show the outstanding performance of the proposed SPFEM, the progressive failure of slope of sensitive clay, one of typical problems in geotechnical engineering involving large deformation, is simulated.

In the region covered by sensitive clays, the progressive landslides generally occur in gently inclined slopes, as observed in Scandinavia and eastern Canada [61]. To illustrate the ability of the proposed method for modelling such a geohazard, the sensitive clay deposit is considered shown in Fig. 16.

According to Locat et al. [61], theses ground movements for progressive landslides occur rapidly and failure propagates in essentially undrained condition. Moreover, these landslides occur in sensitive clays exhibiting a strong strain-softening behaviour during undrained shearing. Therefore, to well simulate such progressive landslides, a modified Mohr-Coulomb model considering strain softening proposed by Yerro et al. [62] is adopted. Based on classical Mohr-Coulomb model, the softening behaviour is achieved by reducing the effective strength parameters (friction angle, ϕ, and cohesion, c) with the accumulated equivalent plastic strain $\varepsilon_{\mathrm{eq}}^{p}$ according to the following exponential softening rules:

$$\begin{cases} c = c_r + \left(c_p - c_r\right) e^{-\eta \varepsilon_{\mathrm{eq}}^p} \\ \phi = \phi_r + \left(\phi_p - \phi_r\right) e^{-\eta \varepsilon_{\mathrm{eq}}^p} \end{cases} \tag{13}$$

where the subscripts "r" and "p" represent the residual and peak values, respectively; η is shape factor to control the rate of degradation. The equivalent plastic strain $\varepsilon_{\mathrm{eq}}^p$ is defined as

$$\varepsilon_{\mathrm{eq}}^p = \sqrt{\frac{2}{3}\mathbf{e}^p : \mathbf{e}^p} \tag{14}$$

where **e** is the deviatoric strain tensor.

For soft sensitive clay, the following parameters according to Zhang et al. [20] are adopted in the simulation: Young's modulus E=1×10^3 kPa, friction angle ϕ=0° assuming undrained shear strength fully taking by the cohesion, dilatancy angle ψ=0°, peak cohesion c_{p}=22 kPa and residual cohesion c_{r}=1.2 kPa, shape factor η=5 which is approximately equivalent to the value of linear reduction relationship adopted by Zhang et al. [20] and Wang et al. [63]. The soil density is ρ =1.7×10^3 kg/m^3. To achieve an approximate undrained condition, the Poisson's ratio υ is set to 0.49 as used by Tran and Sołowski [64] in MPM simulation of retrogressive slope failure. The frictional coefficient μ between the sensitive clay and the rigid bottom surface is set to 0.3, in consistent with the value used by Wang et al. [63]. The initial stress was generated by gravity loading with the earth pressure coefficient K_0=0.5. A total of 3551 particles (6778 3-node triangular elements) are used to discretise the initial problem domain. The maximum size of element is 0.2 m, which is fine enough to get a reasonable phenomenon according to Tran and Sołowski [64]. The initial time step is 0.001 s and the simulation proceeds until the final deposit is obtained.

The collapse process and development of retrogressive failures within the slope is illustrated in Fig. 17, with the coloured contours representing to the accumulated equivalent plastic strain. In practice, the collapse is triggered by removing the soil of toe which may be caused by erosion or excavation [61]. As illustrated, with the first retrogressive collapse moving far away from the new slip surface, the second retrogressive collapse occurs, and then the third retrogressive collapse follows. Due to the friction between collapse and ground, the retrogressive collapse cannot occur infinitely. When a considerable amount of mass is deposited in front of the new slope surface, the

further retrogressive collapse will stop. The final configuration of the slope, shown in Fig. 17(i), indicates that most of the clay involved in collapses has been remoulded. Eventually, the retrogressive failure results in a deposit with a run-out distance of 22.49 m and a retrogression distance of 18.61 m which is reasonable according to the parametric study of Zhang et al. [20]. Note that the run-out and retrogression distances are affected by the model parameters, the interface friction coefficient, and even the adopted constitutive model.

The presented results indicate that the proposed SPFEM with strain-softening material model can simulate the retrogressive failure. Moreover, the outstanding performance of the proposed SPFEM in dealing with the large deformation geotechnical problems is demonstrated.

4 Conclusions

A novel strain smoothing–based particle finite element method (SPFEM) for analysing geotechnical problems was developed. Within the framework of the original PFEM, a simple and effective edge-based strain smoothing method for 3-node triangular elements was implemented. With the adopted strain smoothing method, the strains of all neighbouring elements were fully used in the strain smoothing process. The advantage of the proposed method is to use very simple lower-order triangular element without suffering volumetric locking via the strain smoothing method, instead of using higher-order triangular element/mixed stabilised formulation in original PFEM. To guarantee the stability of calculation using explicit time integration, the computational algorithm employed an adaptive updating time step ~~and used artificial bulk viscosity of numerical damping~~.

The performance of the proposed SPFEM was first examined by four numerical examples: (1) bar vibrations with elastic material, (2) penetration of strip footing with Tresca material, (3) collapse of aluminium bar column with Mohr–Coulomb material and (4) failure of a homogeneous soil slope, also with Mohr–Coulomb material. Finally, an illustrative numerical example, the progressive failure of slope of sensitive clay, is simulated by the proposed SPFEM with strain-softening material model. All results show that the proposed SPFEM can well solve these typical large deformation problems in geotechnical engineering. ~~Furthermore, since lower-order triangle elements can be used directly, the computational cost is reduced preserving the same calculation accuracy because of less degree of~~

freedom required. Accordingly, SPFEM can be a powerful numerical method for large deformation problems of geotechnics.

Further work will focus on the three-dimensional extension of the method and its application in geotechnical engineering.

Acknowledgements

This research was financially supported by the National Natural Science Foundation of China (Grant No. 51579179); the Research Grants Council (RGC) of Hong Kong Special Administrative Region Government (HKSARG) of China (Grant No.: PolyU R5037-18F, 15209119).

Reference

[1] Jin Y-F, Yin Z-Y, Wu Z-X, Daouadji A. Numerical modeling of pile penetration in silica sands considering the effect of grain breakage. Finite Elements in Analysis and Design 2018; 144(15-29.

[2] Jin Z, Yin Z-Y, Kotronis P, Jin Y-F. Numerical investigation on evolving failure of caisson foundation in sand using the combined Lagrangian-SPH method. Marine Georesources & Geotechnology 2018: 1-13.

[3] Jin Y-F, Yin Z-Y, Wu Z-X, Zhou W-H. Identifying parameters of easily crushable sand and application to offshore pile driving. Ocean Engineering 2018; 154(416-429.

[4] Jin Z, Yin Z-Y, Kotronis P, Jin Y-F. Numerical analysis of a suction bucket penetrating in sand with a combined Lagrangian–SPH approach. Procedia Engineering 2017; 175(189-196.

[5] Dey R, Hawlader B, Phillips R, Soga K. Large deformation finite-element modeling of progressive failure leading to spread in sensitive clay slopes. Géotechnique 2015; 65(8): 657-668.

[6] Dai Z, Huang Y, Cheng H, Xu Q. SPH model for fluid–structure interaction and its application to debris flow impact estimation. Landslides 2017; 14(3): 917-928.

[7] Jin Y-F, Yin Z-Y, Zhou W-H, Huang H-W. Multi-objective optimization-based updating of predictions during excavation. Engineering Applications of Artificial Intelligence 2019; 78(102-123.

[8] Wu Z-X, Yin Z-Y, Jin Y-F, Geng X-Y. A straightforward procedure of parameters determination for sand: a bridge from critical state based constitutive modelling to finite element analysis. European Journal of Environmental and Civil Engineering 2017: 1-23.

[9] Shen S, Wang Z, Cheng W. Estimation of lateral displacement induced by jet grouting in clayey soils. Géotechnique 2017; 67(7): 621-630.

[10] Shen SL, Xu YS. Numerical evaluation of land subsidence induced by groundwater pumping in Shanghai. Canadian Geotechnical Journal 2011; 48(9): 1378-1392.

[11] Jin Y-F, Wu Z-X, Yin Z-Y, Shen JS. Estimation of critical state-related formula in advanced constitutive modeling of granular material. Acta Geotechnica 2017; 12(6): 1329-1351.

[12] Yin Z-Y, Jin Y-F, Shen JS, Hicher P-Y. Optimization techniques for identifying soil parameters in geotechnical engineering: Comparative study and enhancement. International Journal for Numerical and Analytical Methods in Geomechanics 2018; 42(1): 70-94.

[13] Hu Y, Randolph M. A practical numerical approach for large deformation problems in soil. International Journal for Numerical and Analytical Methods in Geomechanics 1998; 22(5): 327-350.

[14] Lucy LB. A numerical approach to the testing of the fission hypothesis. The astronomical journal 1977; 82(1013-1024.

[15] Belytschko T, Lu YY, Gu L. Element - free Galerkin methods. International Journal for Numerical Methods in Engineering 1994; 37(2): 229-256.

[16] Harlow FH. The particle-in-cell computing method for fluid dynamics. Methods Comput Phys 1964; 3(319-343.

[17] Oñate E, Idelsohn SR, Del Pin F, Aubry R. The particle finite element method—an overview. International Journal of Computational Methods 2004; 1(02): 267-307.
[18] Hamann T, Qiu G, Grabe J. Application of a Coupled Eulerian–Lagrangian approach on pile installation problems under partially drained conditions. Computers and Geotechnics 2015; 63(279-290.
[19] Qiu G, Henke S, Grabe J. Application of a Coupled Eulerian–Lagrangian approach on geomechanical problems involving large deformations. Computers and Geotechnics 2011; 38(1): 30-39.
[20] Zhang X, Sheng D, Sloan SW, Bleyer J. Lagrangian modelling of large deformation induced by progressive failure of sensitive clays with elastoviscoplasticity. International Journal for Numerical Methods in Engineering 2017; 112(8): 963-989.
[21] Onate E, Idelsohn SR, Celigueta MA, Rossi R. Advances in the particle finite element method for the analysis of fluid–multibody interaction and bed erosion in free surface flows. Computer Methods in Applied Mechanics and Engineering 2008; 197(19-20): 1777-1800.
[22] Oñate E, Celigueta MA, Idelsohn SR, Salazar F, Suárez B. Possibilities of the particle finite element method for fluid–soil–structure interaction problems. Computational Mechanics 2011; 48(3): 307.
[23] Idelsohn SR, Oñate E, Pin FD. The particle finite element method: a powerful tool to solve incompressible flows with free - surfaces and breaking waves. International Journal for Numerical Methods in Engineering 2004; 61(7): 964-989.
[24] Larese A, Rossi R, Oñate E, Idelsohn S. Validation of the particle finite element method (PFEM) for simulation of free surface flows. Engineering Computations 2008; 25(4): 385-425.
[25] Yuan W-H, Wang B, Zhang W, Jiang Q, Feng X-T. Development of an explicit smoothed particle finite element method for geotechnical applications. Computers and Geotechnics 2019; 106(42-51.
[26] Zhang W, Yuan W, Dai B. Smoothed Particle Finite-Element Method for Large-Deformation Problems in Geomechanics. International Journal of Geomechanics 2018; 18(4): 04018010.
[27] Zhang X, Krabbenhoft K, Sheng D. Particle finite element analysis of the granular column collapse problem. Granular Matter 2014; 16(4): 609-619.
[28] Zhang X, Krabbenhoft K, Sheng D, Li W. Numerical simulation of a flow-like landslide using the particle finite element method. Computational Mechanics 2015; 55(1): 167-177.
[29] Zhang X, Oñate E, Torres SAG, Bleyer J, Krabbenhoft K. A unified Lagrangian formulation for solid and fluid dynamics and its possibility for modelling submarine landslides and their consequences. Computer Methods in Applied Mechanics and Engineering 2018.
[30] Carbonell JM, Oñate E, Suárez B. Modeling of ground excavation with the particle finite-element method. Journal of engineering mechanics 2009; 136(4): 455-463.
[31] Salazar F, Irazábal J, Larese A, Oñate E. Numerical modelling of landslide - generated waves with the particle finite element method (PFEM) and a non - Newtonian flow model. International Journal for Numerical and Analytical Methods in Geomechanics 2016; 40(6): 809-826.

[32] Cremonesi M, Ferri F, Perego U. A basal slip model for Lagrangian finite element simulations of 3D landslides. International Journal for Numerical and Analytical Methods in Geomechanics 2017; 41(1): 30-53.
[33] Monforte L, Carbonell JM, Arroyo M, Gens A. Performance of mixed formulations for the particle finite element method in soil mechanics problems. Computational Particle Mechanics 2017; 4(3): 269-284.
[34] Zhang X, Sloan SW, Oñate E. Dynamic modelling of retrogressive landslides with emphasis on the role of clay sensitivity. International Journal for Numerical and Analytical Methods in Geomechanics 2018; 42(15): 1806-1822.
[35] Liu G-R, Trung NT. Smoothed finite element methods: CRC press, 2016.
[36] Cervera M, Chiumenti M, Codina R. Mixed stabilized finite element methods in nonlinear solid mechanics: Part ii: Strain localization. Computer Methods in Applied Mechanics and Engineering 2010; 199(37-40): 2571-2589.
[37] White JA, Borja RI. Stabilized low-order finite elements for coupled solid-deformation/fluid-diffusion and their application to fault zone transients. Computer Methods in Applied Mechanics and Engineering 2008; 197(49-50): 4353-4366.
[38] Liu G, Dai K, Nguyen TT. A smoothed finite element method for mechanics problems. Computational Mechanics 2007; 39(6): 859-877.
[39] Lee C, Lee P-S. A new strain smoothing method for triangular and tetrahedral finite elements. Computer Methods in Applied Mechanics and Engineering 2018; 341(939-955.
[40] Zeng W, Liu G. Smoothed finite element methods (S-FEM): an overview and recent developments. Archives of Computational Methods in Engineering 2018; 25(2): 397-435.
[41] Meduri S, Cremonesi M, Perego U. An efficient runtime mesh smoothing technique for 3D explicit Lagrangian free - surface fluid flow simulations. International Journal for Numerical Methods in Engineering 2019; 117(4): 430-452.
[42] Cremonesi M, Meduri S, Perego U, Frangi A. An explicit Lagrangian finite element method for free-surface weakly compressible flows. Computational Particle Mechanics 2017; 4(3): 357-369.
[43] Belytschko T, Chiapetta R, Bartel H. Efficient large scale non - linear transient analysis by finite elements. International Journal for Numerical Methods in Engineering 1976; 10(3): 579-596.
[44] Hibbitt K, Karlsson B, Sorensen P. ABAQUS/Explicit user's manual (version 10.0). Hibbitt, Karlsson & Sorensen, Inc., Pawtucket, RI, 2002.
[45] Zienkiewicz OC, Zhu JZ. The superconvergent patch recovery and a posteriori error estimates. Part 1: The recovery technique. International Journal for Numerical Methods in Engineering 1992; 33(7): 1331-1364.
[46] Clausen J, Damkilde L, Andersen L. An efficient return algorithm for non-associated plasticity with linear yield criteria in principal stress space. Computers & Structures 2007; 85(23-24): 1795-1807.
[47] Monforte L, Arroyo M, Carbonell JM, Gens A. Numerical simulation of undrained insertion problems in geotechnical engineering with the Particle Finite Element Method (PFEM). Computers and Geotechnics 2017; 82(144-156.

[48] Sołowski W, Sloan S. Evaluation of material point method for use in geotechnics. International Journal for Numerical and Analytical Methods in Geomechanics 2015; 39(7): 685-701.
[49] Kardani M, Nazem M, Carter J, Abbo A. Efficiency of high-order elements in large-deformation problems of geomechanics. International Journal of Geomechanics 2014; 15(6): 04014101.
[50] Silva MVD, Krabbenhoft K, Lyamin AV, Sloan SW. Rigid-plastic large-deformation analysis of geotechnical penetration problems. Proceedings of 13th IACMAG conference2011. p. 42-47.
[51] Prandtl L. Hauptaufsätze: Über die Eindringungsfestigkeit (Härte) plastischer Baustoffe und die Festigkeit von Schneiden. ZAMM - Journal of Applied Mathematics and Mechanics / Zeitschrift für Angewandte Mathematik und Mechanik 1921; 1(1): 15-20.
[52] Meyerhof GG. The Ultimate Bearing Capacity of Foudations. Geotechnique 1951; 4(4): 301-332.
[53] Sołowski WT, Sloan SW. Evaluation of material point method for use in geotechnics. International Journal for Numerical and Analytical Methods in Geomechanics 2015; 39(7): 685-701.
[54] Kardani M, Nazem M, Carter JP, Abbo AJ. Efficiency of high-order elements in large-deformation problems of geomechanics. International Journal of Geomechanics 2015; 15(6): 04014101.
[55] Qiu G, Henke S, Grabe J. Applications of Coupled Eulerian-Lagrangian method to geotechnical problems with large deformations. Proceeding of SIMULIA customer conference2009. p. 420-435.
[56] Bui HH, Fukagawa R, Sako K, Ohno S. Lagrangian meshfree particles method (SPH) for large deformation and failure flows of geomaterial using elastic–plastic soil constitutive model. International Journal for Numerical and Analytical Methods in Geomechanics 2008; 32(12): 1537-1570.
[57] Fern EJ, Soga K. The role of constitutive models in MPM simulations of granular column collapses. Acta Geotechnica 2016; 11(3): 659-678.
[58] Yin Z-Y, Jin Z, Kotronis P, Wu Z. A novel SPH-SIMSAND based approach for modelling of granular collapse. International Journal of Geomechanics 2018.
[59] Bui HH, Fukagawa R, Sako K, Ohno S. Lagrangian meshfree particles method (SPH) for large deformation and failure flows of geomaterial using elastic-plastic soil constitutive model. International Journal for Numerical and Analytical Methods in Geomechanics 2008; 32(12): 1537-1570.
[60] Griffiths D, Lane P. Slope stability analysis by finite elements. Géotechnique 1999; 49(3): 387-403.
[61] Locat A, Leroueil S, Bernander S, Demers D, Jostad HP, Ouehb L. Progressive failures in eastern Canadian and Scandinavian sensitive clays. Canadian Geotechnical Journal 2011; 48(11): 1696-1712.
[62] Yerro A. MPM modelling of landslides in brittle and unsaturated soils: Ph. D. thesis, Universitat Politècnica de Catalunya, 2015.
[63] Wang B, Vardon P, Hicks M. Investigation of retrogressive and progressive slope failure mechanisms using the material point method. Computers and Geotechnics 2016; 78(88-98.

[64] Tran Q-A, Sołowski W. Generalized Interpolation Material Point Method modelling of large deformation problems including strain-rate effects–Application to penetration and progressive failure problems. Computers and Geotechnics 2019; 106(249-265.

Figure captions

Figure 1

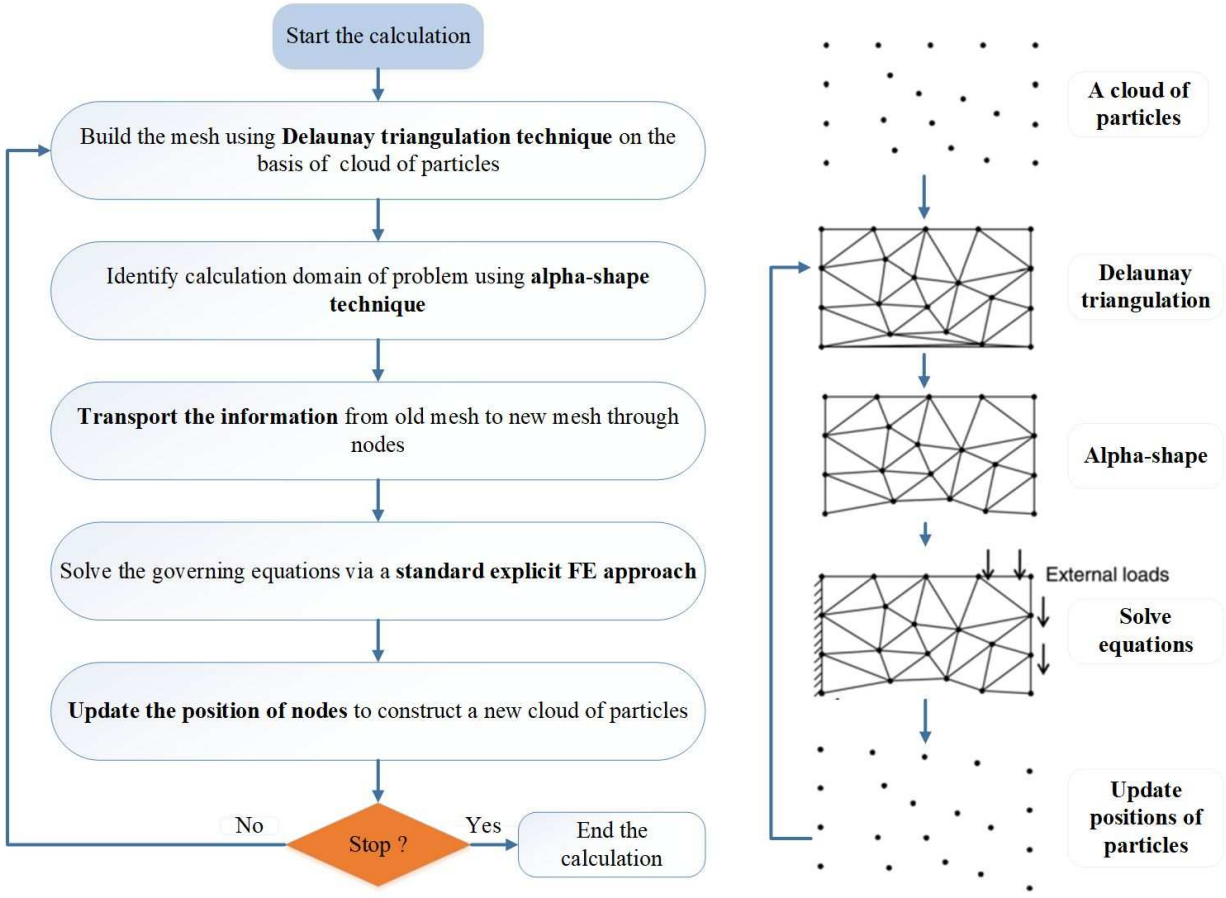

Figure 2

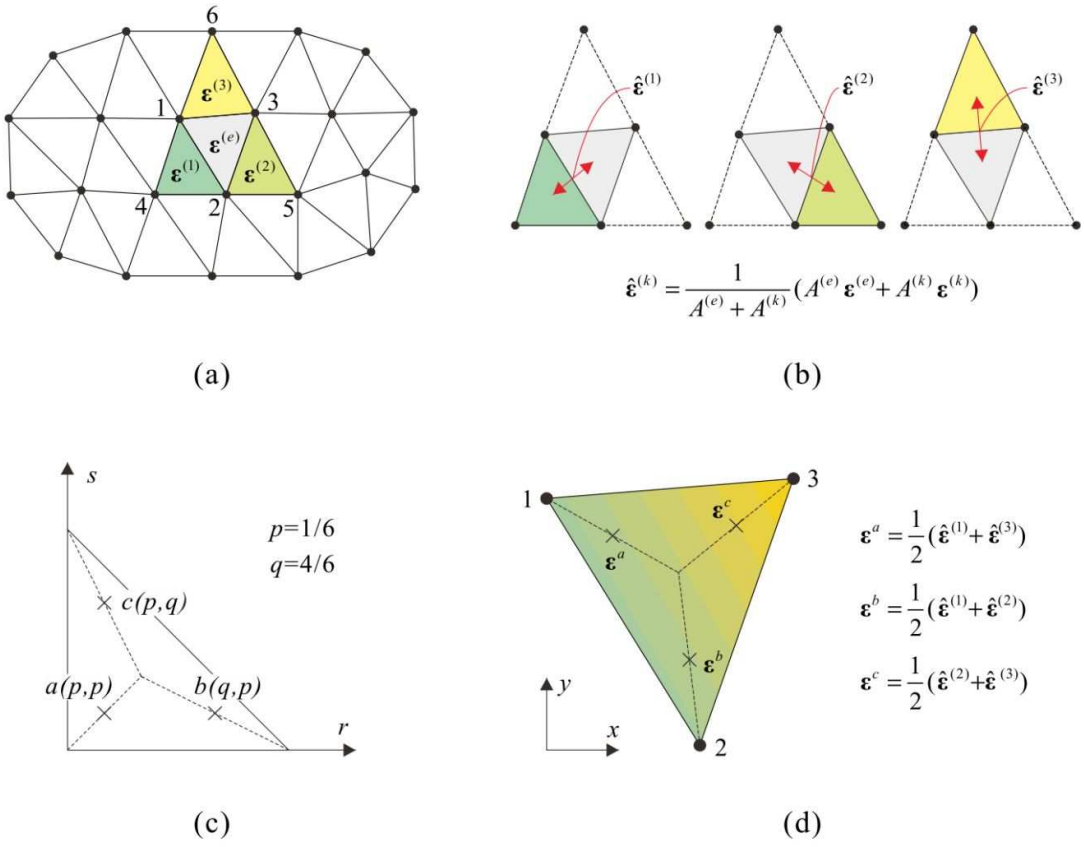

Figure 3

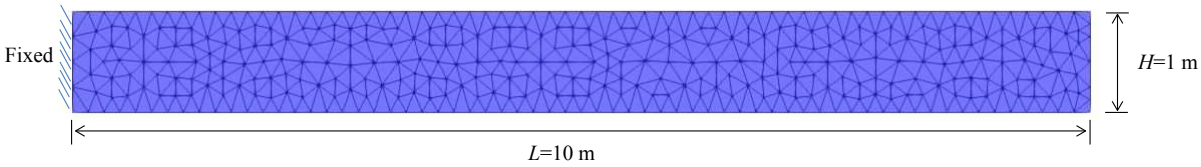

Figure 4

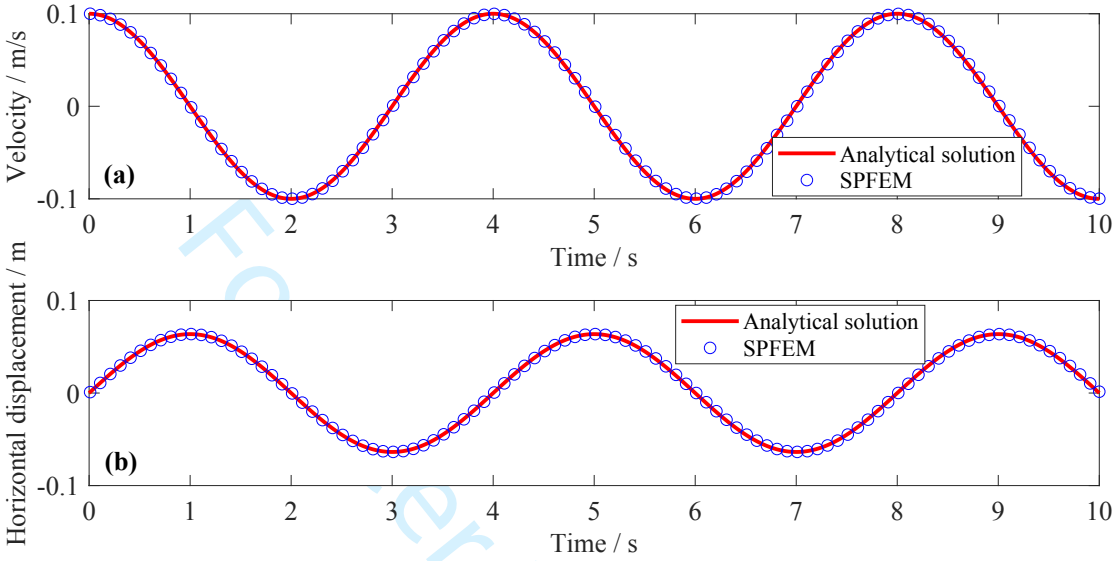

Figure 5

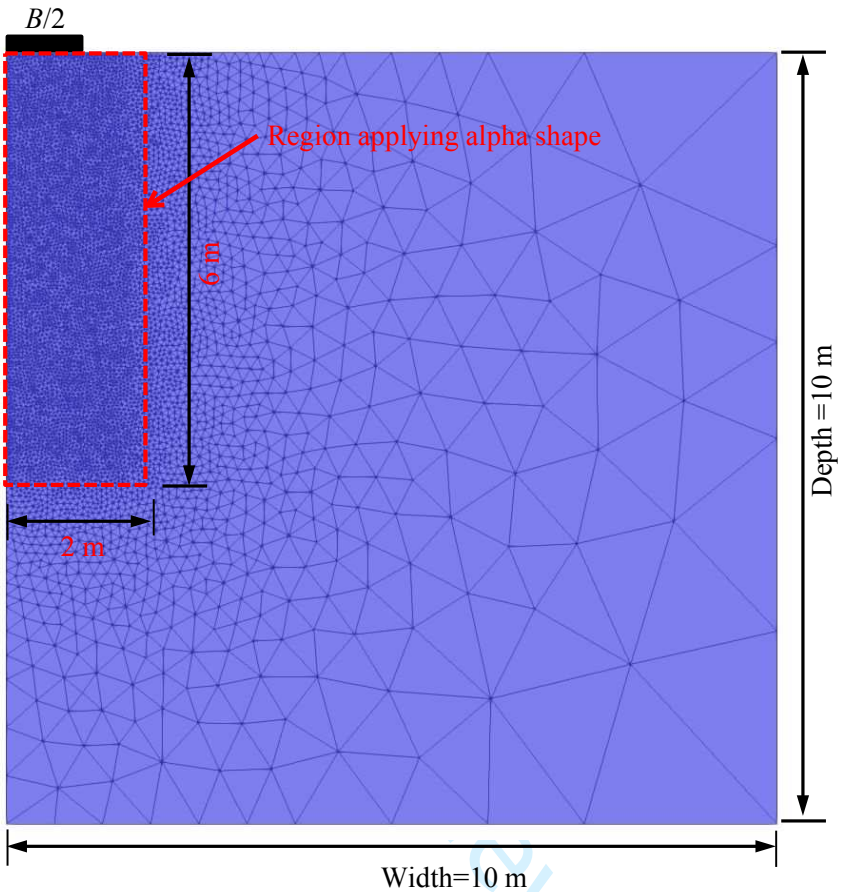

Figure 6

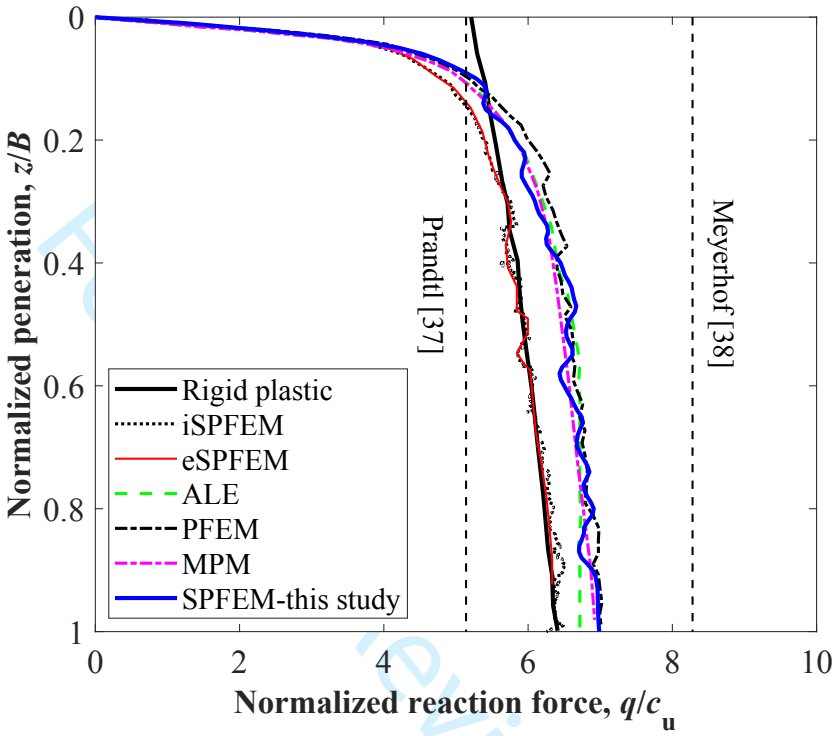

Figure 7

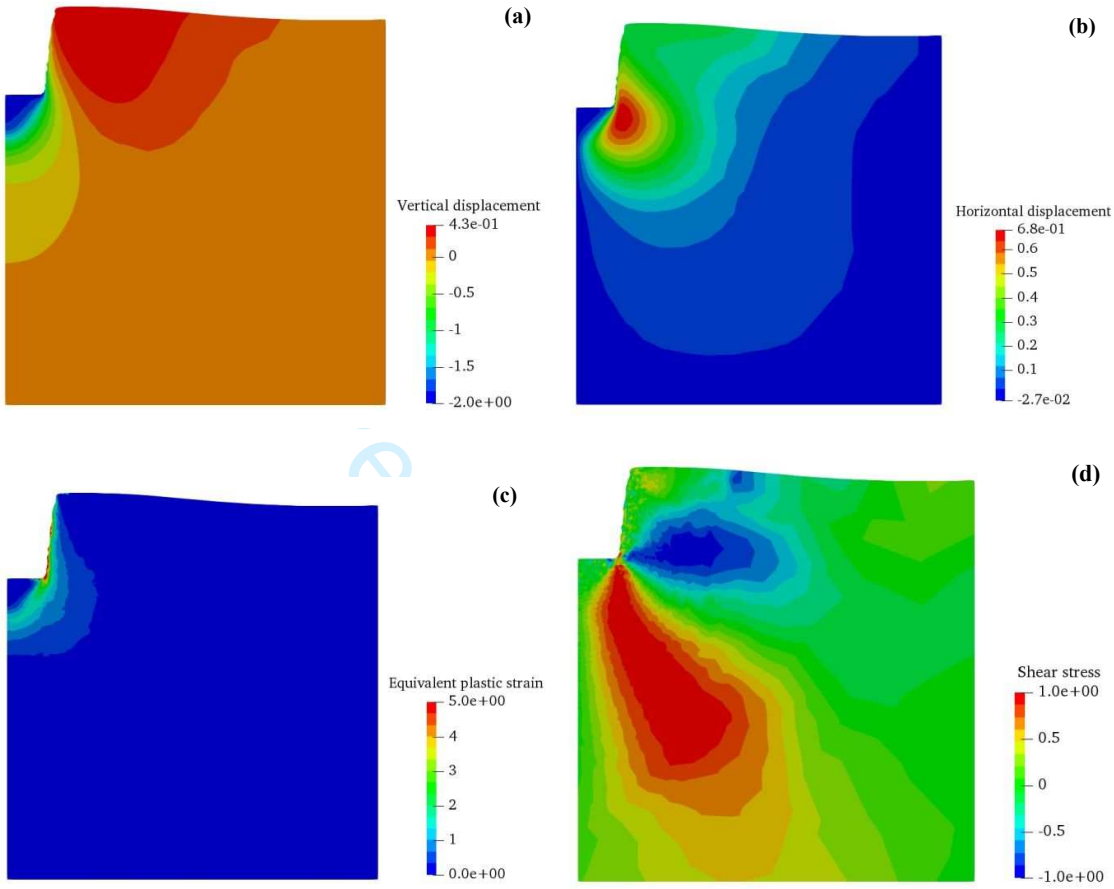

Figure 8

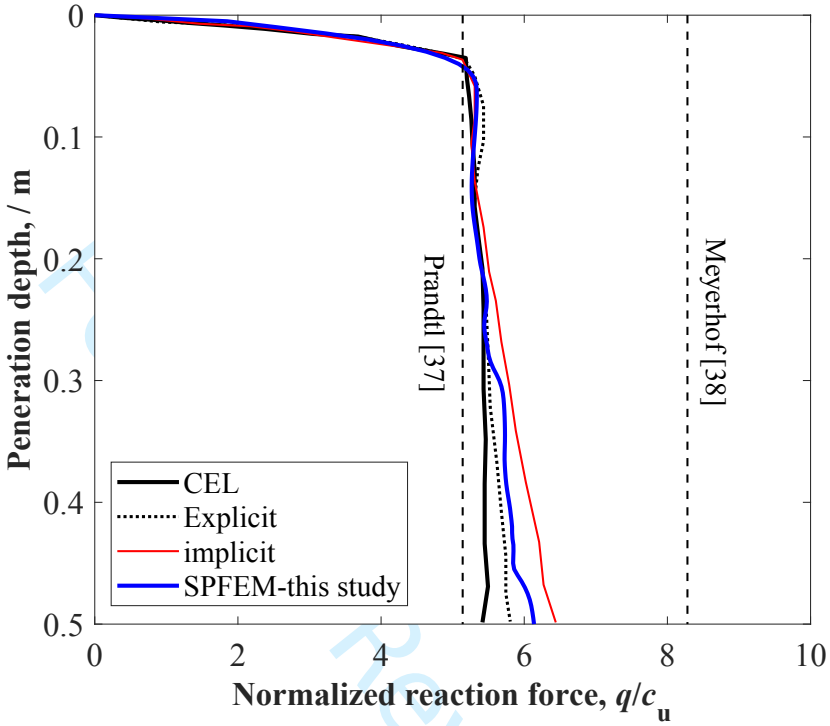

Figure 9

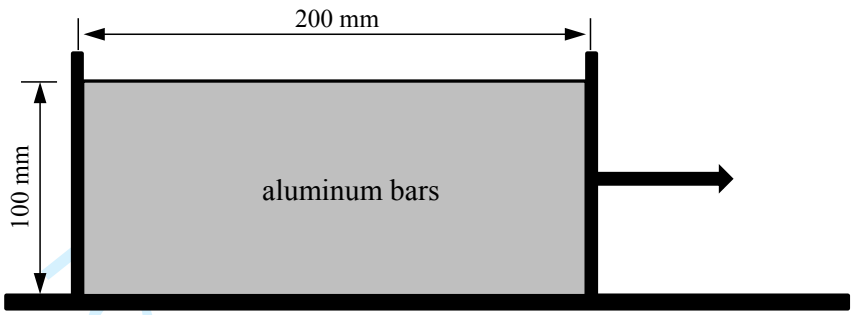

Figure 10

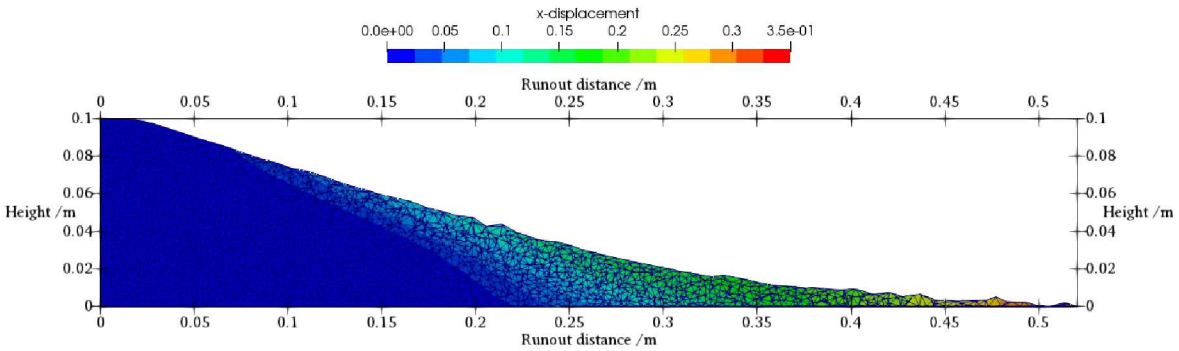
x-displacement
0.0e+00 0.05 0.1 0.15 0.2 0.25 0.3 3.5e-01
Runout distance /m
0 0.05 0.1 0.15 0.2 0.25 0.3 0.35 0.4 0.45 0.5
Height /m
0.1 0.08 0.06 0.04 0.02 0
Runout distance /m

(a)

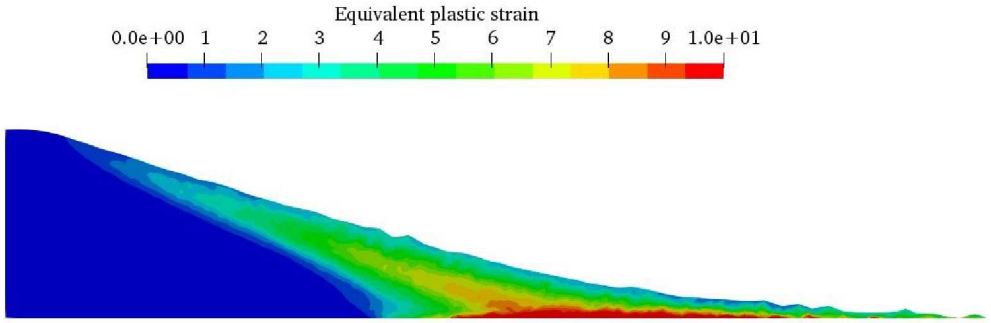
Equivalent plastic strain
0.0e+00 1 2 3 4 5 6 7 8 9 1.0e+01

(b)

Figure 11

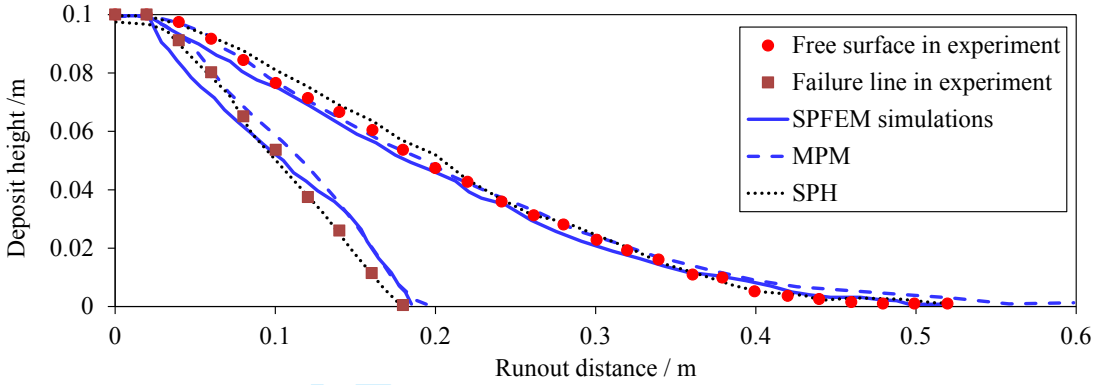

Figure 12

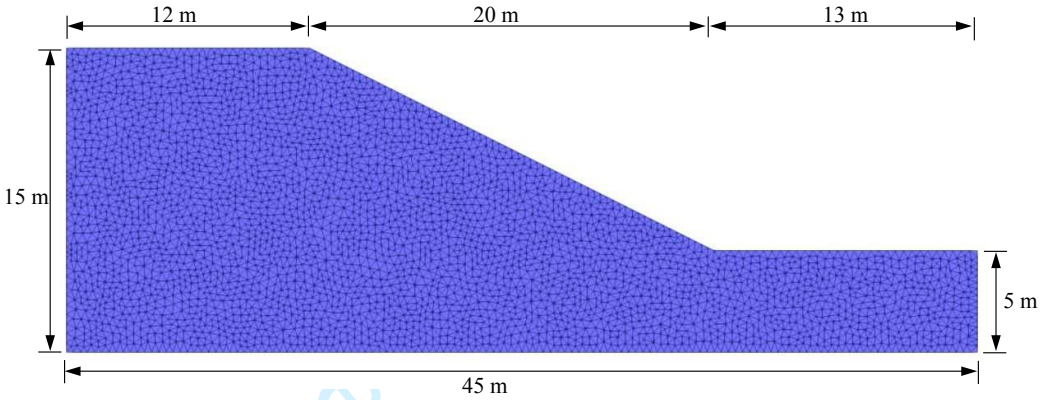

Figure 13

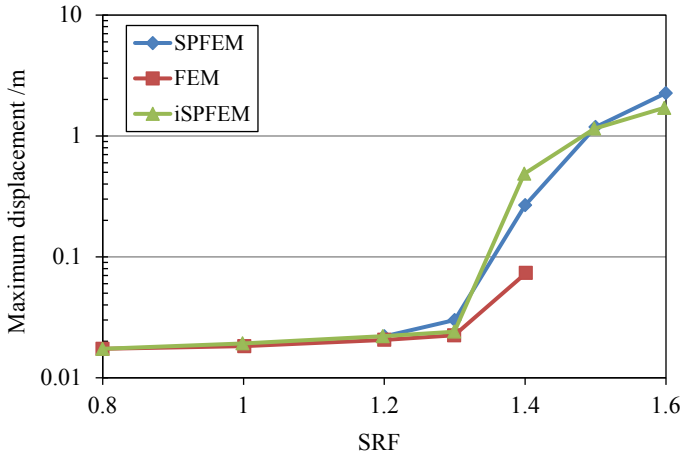

Figure 14

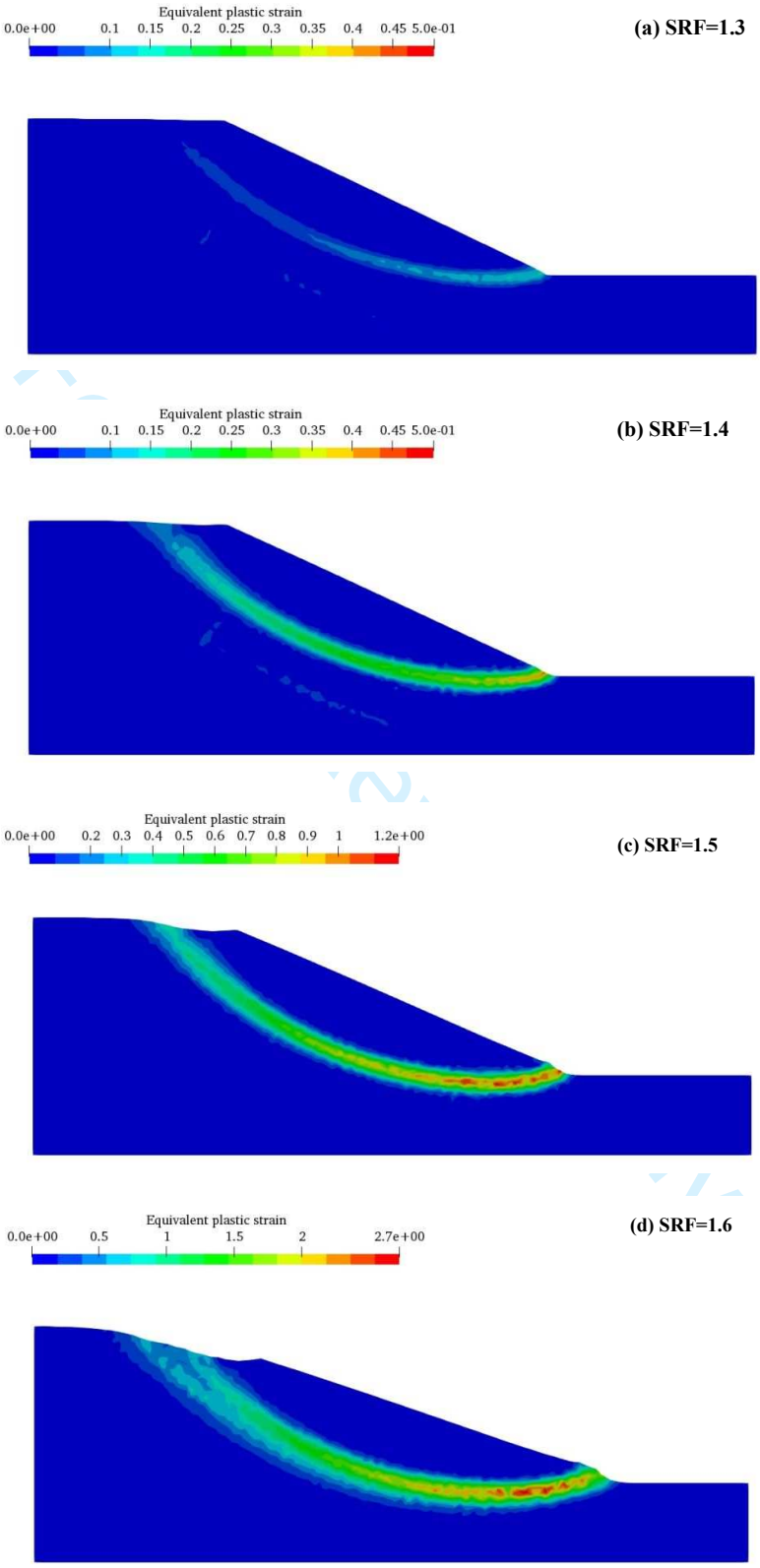
Equivalent plastic strain
0.0e+00 0.1 0.15 0.2 0.25 0.3 0.35 0.4 0.45 5.0e-01
(a) SRF=1.3
Equivalent plastic strain
0.0e+00 0.1 0.15 0.2 0.25 0.3 0.35 0.4 0.45 5.0e-01
(b) SRF=1.4
Equivalent plastic strain
0.0e+00 0.2 0.3 0.4 0.5 0.6 0.7 0.8 0.9 1 1.2e+00
(c) SRF=1.5
Equivalent plastic strain
0.0e+00 0.5 1 1.5 2 2.7e+00
(d) SRF=1.6

Figure 15

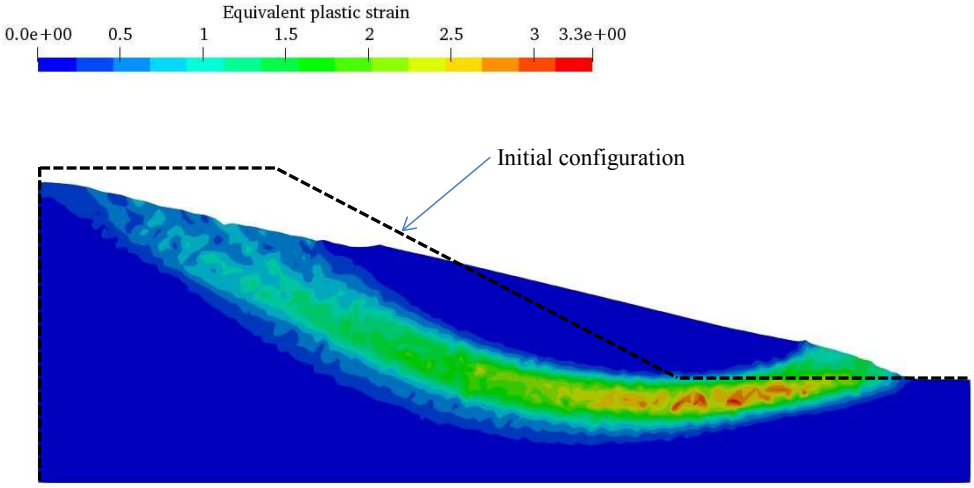

Figure 16

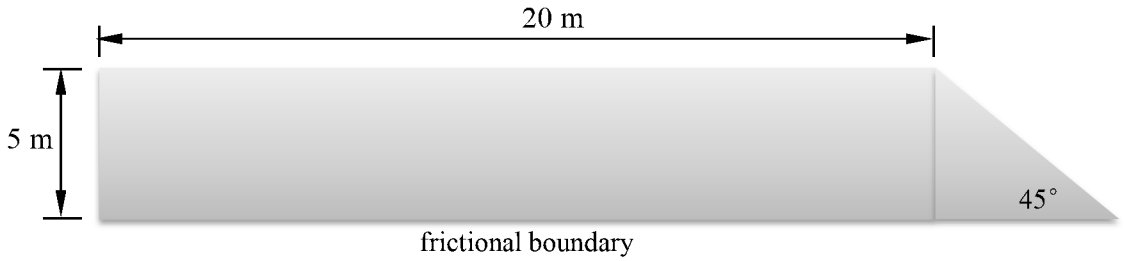

Figure 17

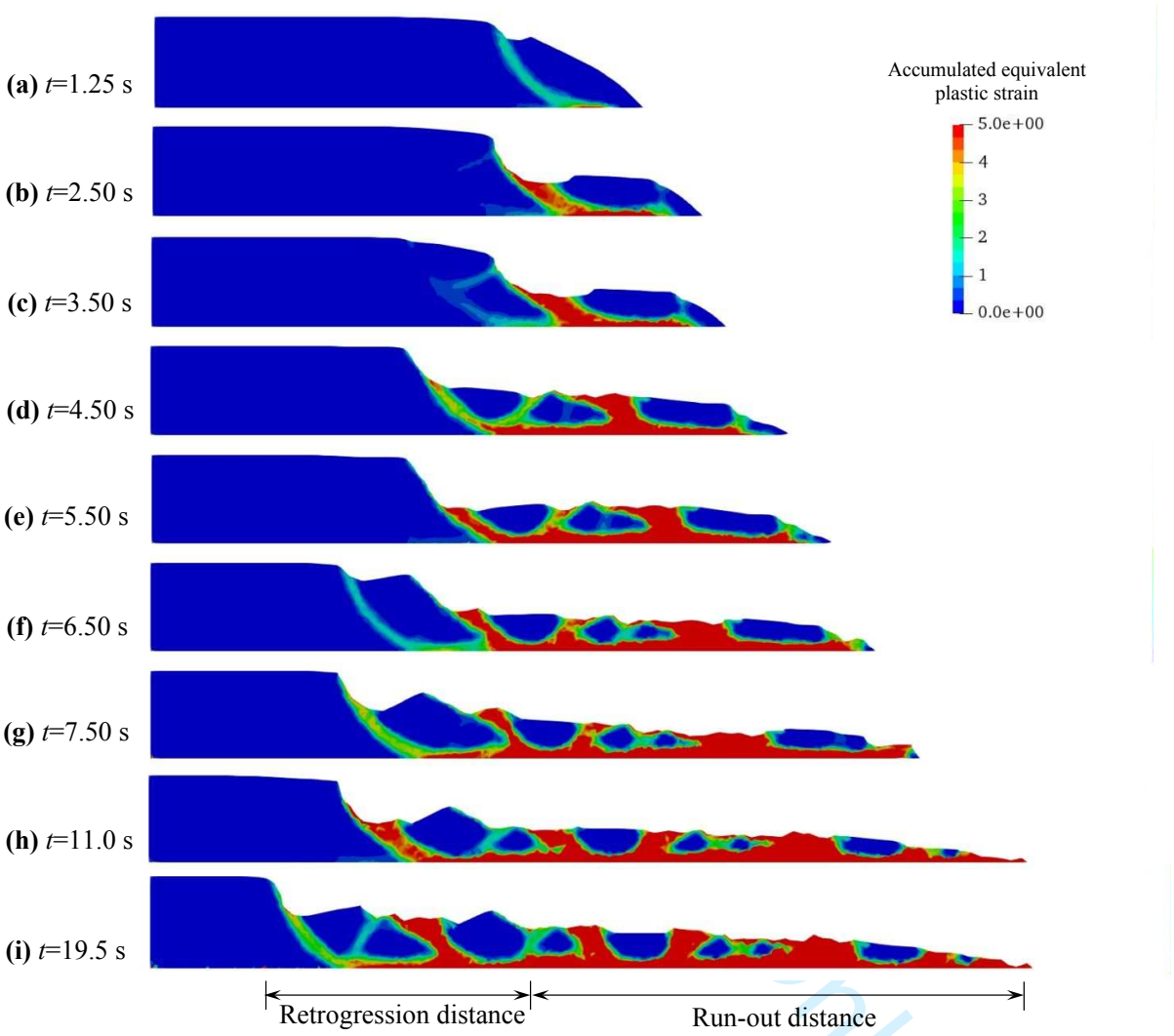
(a) t=1.25 s
(b) t=2.50 s
(c) t=3.50 s
(d) t=4.50 s
(e) t=5.50 s
(f) t=6.50 s
(g) t=7.50 s
(h) t=11.0 s
(i) t=19.5 s
Accumulated equivalent plastic strain
5.0e+00
4
3
2
1
0.0e+00
Retrogression distance
Run-out distance